NANO LETTERS
Letter
Cite This: Nano Lett. 2018, 18, 7794−7800
pubs.acs.org/NanoLett

Opto-Mechanics Driven Fast Martensitic Transition in Two-Dimensional Materials

Jian Zhou,[†,‡] Haowei Xu,[†] Yifei Li,[§] R. Jaramillo,[§] and Ju Li*[,†,§]

[†]Department of Nuclear Science and Engineering, Massachusetts Institute of Technology, Cambridge, Massachusetts 02139, United States

[‡]Center for Advancing Materials Performance from the Nanoscale, State Key Laboratory for Mechanical Behavior of Materials, Xi'an Jiaotong University, Xi'an 710049, China

[§]Department of Materials Science and Engineering, Massachusetts Institute of Technology, Cambridge, Massachusetts 02139, United States

Supporting Information

ABSTRACT: Diffusional phase-change materials, such as Ge−Sb−Te alloys, are used in rewritable nonvolatile memory devices. But the continuous pursuit of readout/write speed and reduced energy consumption in miniaturized devices calls for an optically driven, diffusionless phase change scheme in ultrathin materials. Inspired by optical tweezers, in this work, we illustrate theoretically and computationally that a linearly polarized laser pulse with selected frequency can drive an ultrafast diffusionless martensitic phase transition of two-dimensional ferroelastic materials such as SnO and SnSe monolayers, where the unit-cell strain is tweezed as a generalized coordinate that affects the anisotropic dielectric function and electromagnetic energy density. At laser power of 2.0×10^{10} and 7.7×10^{9} W/cm^2, the transition potential energy barrier vanishes between two 90°-orientation variants of ferroelastic SnO and SnSe monolayer, respectively, so displacive domain switching can occur within picoseconds. The estimated adiabatic thermal limit of energy input in such optomechanical martensitic transition (OMT) is at least 2 orders of magnitude lower than that in Ge−Sb−Te alloy.

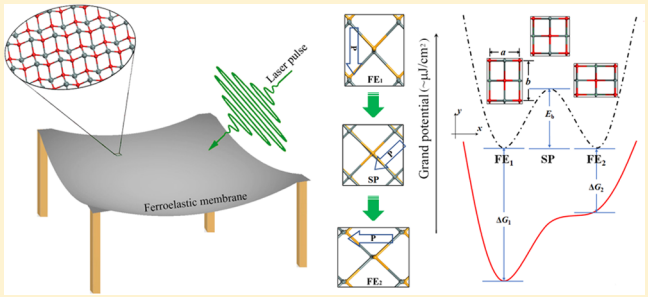

KEYWORDS: *Opto-mechanics, martensitic phase transition, ferroelasticity/ferroelectricity, two-dimensional materials, density functional theory, dielectric function*

Storing and reading information in an efficient, fast, and reversible way with low energy consumption are of great importance. Currently, the most widely used structural phase change material for nonvolatile memory is Ge−Sb−Te alloy,[1] which can exist in both crystalline and amorphous phases with pronounced differences in electrical and optical properties. Upon heating, these two phases can be reversibly switched on a time scale of 10 to 100 ns by diffusion of atoms. This order−disorder transition has a latent heat and requires breaking of chemical bonds. It is highly desirable to explore new phase-change materials with degenerate, diffusionless order-to-order transitions to accelerate the read/write kinetics, reduce energy dissipation, and eliminate fatigue.

Since the isolation of graphene sheet in 2004,[2] two-dimensional (2D) materials with a few atomic layers thickness (e.g., hexagonal boron nitride,[3] transition-metal dichalcogenides,[4] and phosphorene[5]) have been developed rapidly.[6−12] Some layered 2D materials (such as MoS_2 and analogues) have been found to possess multiple (meta-)stable structural phases or orientation variants, holding the possibility to function as nonvolatile phase change memory materials with reduced size. For example, previous predictions have revealed that carrier doping, electrostatic gating, or tensile strain can induce phase transformation of $MoTe_2$ monolayer (and similar materials) between 2H and 1T′ structures, or transition among different orientations in the 1T′ phase.[13−15] Such transitions have also been experimentally verified.[16] Subsequent theoretical calculations also suggested that these 2D phase transformation can further decrease the required operation energy over the Ge−Sb−Te alloys.[17] However, these methods typically require mechanical, electrical, or electrochemical contacts and patterning. Optical readout/write with focused laser would be preferable in many circumstances, especially for 2D materials which are easily optically accessible. For example, the photostrictive property has been observed in $BiFeO_3$, where there was a relative elongation of 10^{-5} when irradiated by a laser light of 70 kW/m^2.[18]

Martensitic transitions are displacive, without the need for random diffusions of atoms which are thermally driven. Hence,

Received: September 3, 2018
Revised: November 5, 2018
Published: November 6, 2018

DOI: 10.1021/acs.nanolett.8b03559
Nano Lett. 2018, 18, 7794−7800

the time scale of transformation can be greatly reduced. In this study, we propose a photonic energy-assisted approach that could induce optomechanical martensitic transitions (OMT) of 2D ferroelastic (FE) materials. OMT differ from temperature-driven martensitic transitions (MT, e.g., in steel heat-treatment) in that the photonic energy couples strongly to only one generalized reaction coordinate ξ, and not with the other degrees of freedom, thus breaking the equi-partition character of a temperature-driven process. The benefit of laser scanning read/write compared to static electric field switching is the easy spatial addressability. Because 2D ferroelastic domains are unconstrained in the z-direction, the elastic energy required for switching is much reduced compared to that in 3D MT systems. Several 2D FE materials have been discovered.[15,19,20] FE materials exhibit spontaneous symmetry-breaking strains (transformation strains) and consequently have at least two degenerate orientation variants, and the switching between these orientation variants is diffusionless.

Here we focus on recently discovered SnO and SnSe monolayers.[19,20] Because the two 90°-orientation variants of ferroelastic SnSe and SnO have rectangular symmetry, alternating electric field along different polarization directions will bias the variants differently. Hence, we predict that one can use a short pulse of linearly polarized light (LPL) to induce a phase transition from one orientation variant to the other. For example, a monolayer SnSe nanosheet with a lateral size of $L \sim 300$ nm has been fabricated via a colloidal route,[21] SnO monolayer has also been grown using a liquid metal van der Waals exfoliation technique,[22] and such size could be ideal for wholesale-switching in freely suspended mode (with slight prebuckling in both x and y to give it some "slack"—zeroing tensile stresses and removing the in-plane elasticity constraints as well). By first-principles calculations, we show that the optical-frequency dielectric responses along different directions in these anisotropic FE monolayers exhibit a large orientational contrast. Like optical tweezers that can change the spatial coordinates of a dielectric bead using the dielectric energy of the laser-bead interaction, in this case the unit-cell geometry (strain and internal atomic shuffling coordinates[23]) as a generalized coordinate ξ, upon which the dielectric constant ε depends. The dielectric energy (proportional to $E^2\varepsilon(\xi)$ where E is the electric field amplitude) modifies the potential energy landscape of the martensitic transition. At a critical laser power this dielectric energy causes the transition barrier (measured in energy/area) to vanish across the entire sample, leading to barrier-free OMT. When this happens, one can avoid the typical nucleation-and-growth kinetics, and the transition can happen dynamically within picoseconds everywhere across the whole sample. Because the freely suspended sample is slightly prebuckled, there will be no tensile transformation stress or long-range elasticity constraint in x, y, or z, which is fundamentally different from the general case of 3D MT. Even though the required pulsed laser power may be high, the extremely fast transition will cause the total heat absorption to be small, allowing efficient and damage-free operation.

We show our schematic setup of FE monolayer transformation under LPL exposure in Figure 1a and the typical FE potential energy change in Figure 1b. In a nonpolarized SnO monolayer, a rectangular FE monolayer would have two vertical orientation variants (FE_1 and FE_2), while the saddle point (SP) state with high symmetry serves as an energy barrier to separate the FE_1 and FE_2 orientation variants (black curve in Figure 1b). Each orientation variant is thermodynamically stable and the energies of the different states per supercell satisfy $E_{FE_1} = E_{FE_2} < E_{SP}$. To induce a transition from FE_2 to FE_1 across a sample of linear dimension L, we apply LPL onto the sample. The LPL contains an oscillating electric field (e.g., $\mathbf{E}(\omega_0, t) = Ee^{-i\omega_0 t}\hat{\mathbf{e}}_x$, where $\hat{\mathbf{e}}_x$ is unit vector along the x direction) that accelerates ions and electrons. The thermodynamic fundamental equation can be written as $dU = S \times \mathbf{E}\cdot d\mathbf{P}_0 + S \times \mathbf{E}\cdot d\mathbf{D}$, where U is internal energy and S is total area. Here we have ignored the entropy and stress effects. Under linear approximation and using electric field $\mathbf{E}$ as a natural variable, this induces an additional term in thermodynamical grand potential density (unit energy/area):

$$G(\mathbf{E}) = G(E = 0) - \mathbf{E}\cdot\mathbf{P}_0 - \frac{1}{2}\mathbf{E}^*\cdot\boldsymbol{\varepsilon}^{(1)}(\omega_0)\cdot\mathbf{E} \quad (1)$$

where $\mathbf{P}_0$ is intrinsic static polarization and $\boldsymbol{\varepsilon}^{(1)}(\omega_0)$ is the real part of the dielectric function tensor. The first term is intrinsic grand potential without electric field. The second term vanishes for nonpolarized SnO monolayer FE_1/FE_2, with centrosymmetry even at the ferroelastic state. The third term incorporates the response of both ion and electron subsystems to the electric field ($\boldsymbol{\varepsilon} = \boldsymbol{\varepsilon}_{ion} + \boldsymbol{\varepsilon}_{electron}$). Here we consider the frequency ω_0 on the order of 10^2 terahertz (THz). Considering that phonon frequencies are typically below 20 THz, the ion response ($\boldsymbol{\varepsilon}_{ion}$) to the electric field would be small (see Supporting Information and Figure S1 for detailed discussions) because they are far off-resonance due to the heavy masses of ions. In the following, we will only consider the dielectric function from electron subsystem contribution $\boldsymbol{\varepsilon}_{electron}$. In anisotropic FE 2D materials, the electronic dielectric function tensor components along the x and y directions are not equal ($\varepsilon^{(1)}_{xx} \neq \varepsilon^{(1)}_{yy}$). Therefore, LPL lifts the degeneracy of the FE_1 and FE_2 orientation variants. When the energy difference is sufficiently large, this effect creates a barrier-free OMT from FE_2 to FE_1 (Figure 1b, red curve) that avoids nucleation-and-growth kinetics.

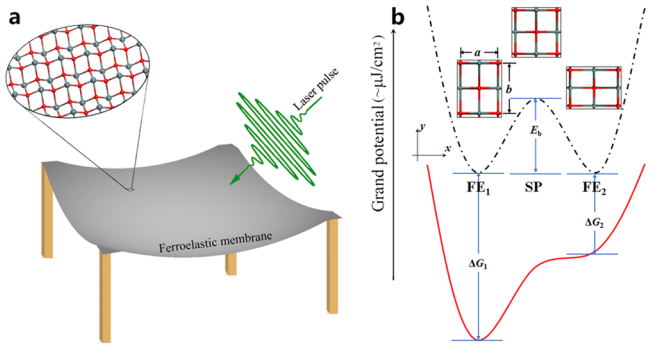

Figure 1. Schematic plot of SnO monolayer phase transition under optical exposure. (a) SnO monolayer under LPL pulse exposure. (b) Elastic energy curve of intrinsic state (no exposure, black dashed dot curve), where FE_1 and FE_2 states are energetically degenerate. LPL lifts the degeneracy of thermodynamic grand potential of FE_1 and FE_2 orientation variants (red solid curve).

In this section, we use density functional theory (DFT,[24,25] see Theoretical Methods) to show that OMT can be realized in FE SnO monolayers. After full relaxation, the SnO monolayer (inset of Figure 1b) shows a FE rectangular unit cell with *pmmn* layer group. The FE state is energetically lower than the high symmetric SP by 0.61 meV per chemical formula unit (f.u.). Taking the SP structure as reference, we calculate that the 2D transformation strain tensor $\boldsymbol{\eta}$ of FE_1 and FE_2 is

DOI: 10.1021/acs.nanolett.8b03559
Nano Lett. 2018, 18, 7794−7800

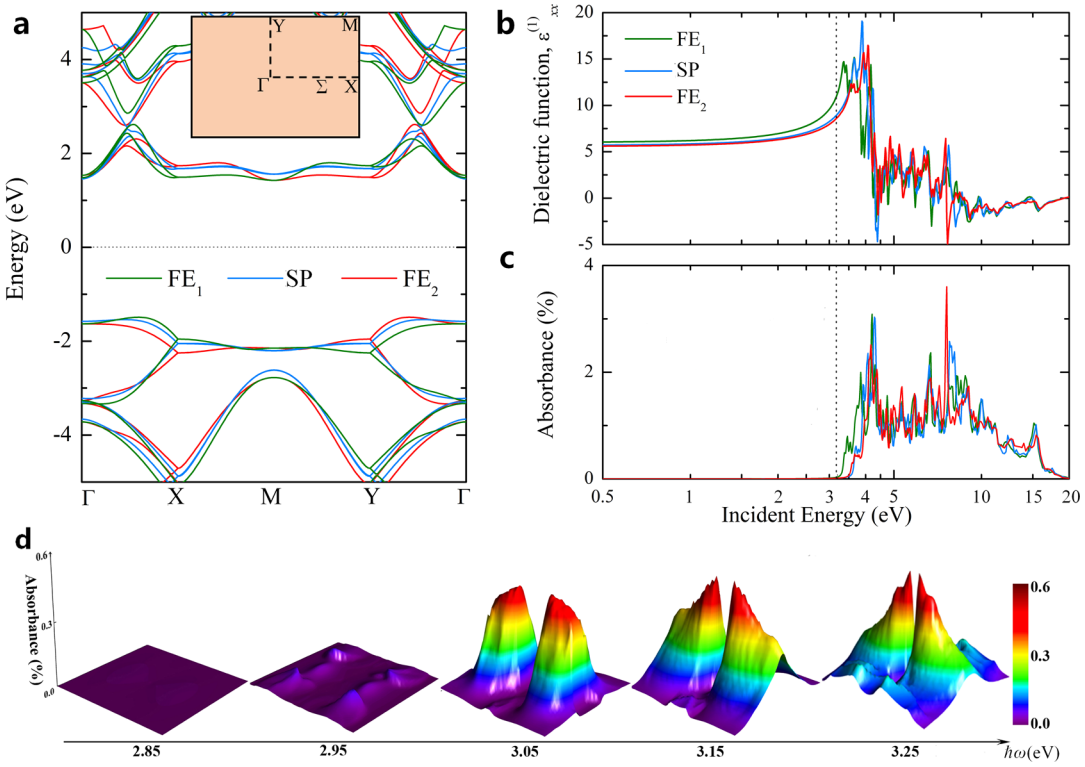

Figure 2. Electronic property of a SnO monolayer. (a) Band dispersions of FE_1, SP, and FE_2 states along high symmetry path in the first Brillouin zone. The direct coordinates are Γ = (0, 0, 0), X = (1/2, 0, 0), M = (1/2, 1/2, 0), and Y = (0, 1/2, 0). Inset shows the first Brillouin zone of FE_1 state. The Fermi level lies in the middle of VBM and CBM (dotted horizontal line at zero energy). (b) RPA calculated real part dielectric function $\varepsilon_{xx}^{(1)}$ and (c) optical absorption spectra at the long wavelength limit. The dashed vertical line denotes energy $\hbar\omega_0$ = 3.25 eV. (d) Optical absorbance in the first Brillouin zone (finite q) in the vicinity of indirect bandgap.

$$\eta_{FE_1} = \begin{pmatrix} -0.048 & 0 \\ 0 & 0.048 \end{pmatrix} \qquad \eta_{FE_2} = \begin{pmatrix} 0.048 & 0 \\ 0 & -0.048 \end{pmatrix} \tag{2}$$

These results agree well with previous work.[19] These transformation strains are sufficiently small that a −5% biaxial prebuckling of a freely suspended sheet (like a hammock) would ensure that no tensile stress will be generated during the OMT. The calculated band dispersions of FE_1, SP, and FE_2 are shown in Figure 2a. We find that the FE SnO monolayer is a quasi-direct bandgap semiconductor. In the FE_1 structure, the valence band maximum (VBM) is along the Γ → X path (Σ = 0.28 × 2π/a, 0, 0), and the conduction band minimum (CBM) is at the corner of Brillouin zone (M = π/a, π/b, 0). This gives an indirect bandgap of 2.92 eV. The direct bandgap is 3.11 eV, corresponding to optical transitions at the Γ point.

We calculate the in-plane optical response using the random phase approximation (RPA). The relative dielectric function (cgs units, ref 26) in the long wavelength limit ($q \to 0$) is

$$\varepsilon_{\alpha\alpha}(\omega) = 1 - \lim_{q\to 0} \frac{4\pi e^2}{q^2}\frac{1}{\Omega}\sum_{c,v,\mathbf{k}} w_{\mathbf{k}} \times \frac{|\langle u_{v,\mathbf{k}}|u_{c,\mathbf{k}+q_\alpha}\rangle|^2}{E_{c,\mathbf{k}} - E_{v,\mathbf{k}} - \hbar\omega - i\zeta} \quad (\alpha = x, y) \tag{3}$$

The indices c and v refer to conduction and valence band states, respectively, and $|u_{n\mathbf{k}}\rangle$ is the cell-periodic part of the wave functions of the band-n at $\mathbf{k}$. Ω is the volume of the simulation supercell, $w_{\mathbf{k}}$ is the weight of each $\mathbf{k}$-point, and ζ is a phenomenological damping parameter taking to be 0.025 eV in our calculation. For 2D materials in a 3D-periodic supercell, one has to eliminate the vacuum contributions and spurious interactions between different periodic image layers. From eq 3, the supercell calculated dielectric function is inversely proportional to d, the thickness of simulating supercell. One scheme that can be used is to truncate Coulomb interactions,[27] which shows vacuum-independent optical response based on 2D electronic screening of Coulomb interaction.[28] Here, we employ another method to rescale the calculated in-plane (x and y) dielectric function, based on 3D electronic screening, which also eliminates the vacuum dependence. The supercell can be regarded as a parallel combination of the 2D SnO monolayer and the vacuum capacitance,[29] so that the real part of 2D SnO monolayer dielectric function satisfies

$$d \times \varepsilon_{\text{cell}}^{(1)} = (d - h) \times \varepsilon_{\text{vac}}^{(1)} + h \times \varepsilon_{\text{2D}}^{(1)} \tag{4}$$

$\varepsilon_{\text{cell}}^{(1)}$, $\varepsilon_{\text{vac}}^{(1)}$, and $\varepsilon_{\text{2D}}^{(1)}$ represent the real parts of dielectric function of the supercell, the vacuum, and the 2D material, respectively. The distance parameters d and h are the thickness of simulating supercell and of the 2D material, respectively. We take the thickness of a SnO monolayer to be the distance between two adjacent layers in bulk SnO, h = 4.276 Å. In this way, the rescaled $\varepsilon_{\text{2D}}^{(1)}$ is independent of the thickness of the simulating supercell.

Optical absorption can be evaluated from the imaginary part of the dielectric function. The absorbance (A) of a 2D material is calculated as

$$A(\omega) = 1 - \exp\left(-\frac{\omega}{c}\varepsilon^{(2)}d\right) \tag{5}$$

DOI: 10.1021/acs.nanolett.8b03559
Nano Lett. 2018, 18, 7794−7800

where c is the speed of light. We plot $\varepsilon^{(1)}_{2D,xx}$ for the three structures FE_1, SP, and FE_2 in Figure 2b, and corresponding absorbance $A(\omega)$ in Figure 2c. There are clear differences in the dielectric functions of the FE_1 and FE_2 variants. We note that ε_{xx} of FE_2 is ε_{yy} of FE_1, due to the structural anisotropy of the FE state. The first absorption peak appears at 3.44 and 3.57 eV for FE_1 and FE_2, respectively. This optical anisotropy can be understood by analyzing the group representations of the frontier orbitals (Table S1 in Supporting Information). Taking the FE_1 structure as the example, by examining the group representations of the highest valence and lowest conduction bands, we find that optical absorption is prohibited at the Γ point. The lowest optical absorption of x-polarized light occurs at the X point (with a direct bandgap of 3.45 eV), and for the y-polarized light it corresponds to the transition at the M point (3.57 eV).

The optical anisotropy suggests that the phase transition between FE_1 to FE_2 could be triggered by LPL. For instance, if one fixes the incident energy at $\hbar\omega_0 = 3.25$ eV (dashed vertical line in Figure 2b and c), the real part dielectric functions in the x-direction satisfy $\varepsilon^{(1)}_{FE_2} < \varepsilon^{(1)}_{SP} < \varepsilon^{(1)}_{FE_1}$. Note that the small dielectric function refers to a low screening effect and high electric field in SnO. Thus, the dielectric energy density in the FE_2 state is larger than those in the SP and FE_1 states. Under a finite intensity of LPL, a phase transition from FE_2 to FE_1 occurs with a reduced energy barrier. We estimate the critical electric field strength of barrier-free phase transition by $-\frac{1}{2}\varepsilon_0\varepsilon^{(1)}_{FE_2}E^2Sh = E_b - \frac{1}{2}\varepsilon_0\varepsilon^{(1)}_{SP}E^2Sh$, where S is the supercell area, ε_0 is the vacuum permittivity, and E_b is the original energy barrier (see Supporting Information for details). Using $\varepsilon^{(1)}_{FE_2} = 8.952$ and $\varepsilon^{(1)}_{SP} = 9.322$, we find that the critical electric field strength is $E_0 = 1.37$ V/nm. We found similar results using many-body GW-BSE calculations[30−33] (see Theoretical Methods). If we choose an incident energy $\hbar\omega_0 = 4.36$ eV (for which $\varepsilon^{(1)}_{FE_2} = 9.86$ and $\varepsilon^{(1)}_{SP} = 14.29$), then the critical electric field strength and laser power can be reduced to $E_0 = 0.39$ V/nm and $I_0 = 2.05 \times 10^{10}$ W/cm^2 (Figure S2 and Table S3 in Supporting Information). This is achievable by visible spectrum pulsed lasers. Note that the self-energy in many-body GW calculations may change the band topology of 2D materials;[34] here we find that the indirect bandgap feature still remains for the SnO monolayer.

To illustrate the OMT process more explicitly, we calculate the total energy as a function of biaxial strain η_{11} (= $-\eta_{22}$) in a SnO monolayer and its corresponding dielectric function in the x-direction (Figure 3). The RPA-calculated $\varepsilon^{(1)}_{xx}(\omega_0)$ decreases from FE_1, to SP, to FE_2. For biaxial strain beyond FE_2 ($\eta_{11} > 0.048$), the $\varepsilon^{(1)}_{xx}(\omega_0)$ increases again. LPL lifts the degeneracy of FE_1 and FE_2, and increasing the laser power causes the transition barrier to decrease and eventually to disappear. Throughout the FE_1 potential well is retained (Figure 3b). Thus, an FE_2 orientation variant can switch to FE_1 simultaneously throughout the sample by optical "tweezing", with no barrier and no elastic energy constraint.

In $Ge_2Sb_2Te_5$ alloys, the adiabatic thermal limit of energy input is estimated to be ~1.17 aJ/nm^3. Recent calculations of phase-transitions in $MoTe_2$ monolayers yield a lower estimate, on the order of 0.1 aJ/nm^3 (ref 17). The lower limit of energy required for OMT can be simply evaluated from internal energy expression, $E_{input} = \frac{1}{2}\varepsilon_0\varepsilon_{FE_2}ShE^2$. This energy is ~16 meV/f.u. (Figure 3b), which converts to 0.07 aJ/nm^3,

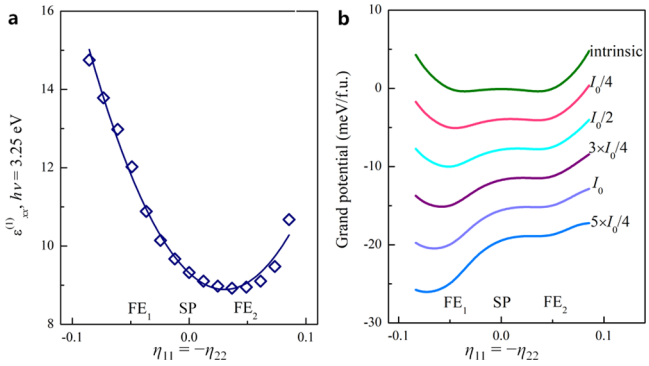

Figure 3. Laser power modulation of energy profile. (a) RPA-calculated real part of dielectric function in the x-direction, at incident energy of 3.25 eV, as a function of strain. (b) Grand potential of SnO monolayer per formula unit vs strain under different laser power. The energy is shifted with respect to the intrinsic (no LPL) SP state.

comparable to the predictions for $MoTe_2$ monolayers. Using the results of GW-BSE calculations, this energy density is further reduced to 0.006 aJ/nm^3. If this energy is dissipated as waste heat, then using the heat capacity of bulk SnO (>4.1 cal/mol K, ref 35), we estimate that the temperature rise is below 11 K.

The barrier-free and diffusionless martensitic phase transition is ultrafast. We analyze its kinetics by taking the total mass of a SnO to be $m = m_{Sn} + m_O = 134$ amu, and a characteristic displacement of $l = (b - a) = 0.32$ Å. The energy change in the transition is $\Delta E = \Delta E_1 - \Delta E_2 = 5.1$ meV/f.u. According to a simplified constant acceleration motion model, the transition time can be approximated to be $\tau = l \times \sqrt{2m/\Delta E} \approx 1.1$ ps. This indicates that the phase transition should occur on the order of picosecond, faster than that in Ge−Sb−Te alloys. Thus, a laser pulse as brief as 10 ps should be sufficient for switching.

The incident photon energy of $\hbar\omega = 3.25$ eV is higher than that of indirect bandgap (2.92 eV) of the SnO monolayer. Therefore, indirect band gap transition may occur at this frequency. In order to evaluate this effect, we fit the band dispersion of SnO monolayer (at the DFT level) by maximally localized Wannier functions,[36] as implemented in the Wannier90 code.[37] Then we use Lindhard theory[38] to calculate the dielectric function at finite q under RPA

$$\varepsilon(\mathbf{q}, \omega) = 1 - \frac{e^2}{\varepsilon_0 q^2}\int \frac{1}{(2\pi)^3}\mathrm{d}\mathbf{k} \sum_{m,n} \frac{(f_{n,\mathbf{k}+\mathbf{q}} - f_{m,\mathbf{k}})\left|\left\langle u_{n,\mathbf{k}+\mathbf{q}}\middle|u_{m,\mathbf{k}}\right\rangle\right|^2}{E_{n,\mathbf{k}+\mathbf{q}} - E_{m,\mathbf{k}} + \hbar\omega - i\zeta} \quad (6)$$

Here f is the Fermi−Dirac distribution. By adjusting the incident $\hbar\omega$ from 2.85 eV (lower than indirect bandgap) to 3.25 eV (incident laser energy), we plot the optical absorbance $A(\mathbf{q}, \omega)$ in the first Brillouin zone (Figure 2d). Below the indirect bandgap, the optical absorbance remains zero in the whole $\mathbf{k}$-space. Once the incident energy exceeds the bandgap, very small absorbance is found. The highest peak locates at the $q = (\pm 0.069, 0, 0) \times$ Å^{-1} point when $\hbar\omega = 3.25$ eV, with absorbance of $A(q, \omega) = 0.57\%$. Such a large q would also require phonon assistance in reality. Thus, we expect marginal indirect bandgap transition occurs in the process, and can be omitted during a short picosecond pulse. In addition, the

DOI: 10.1021/acs.nanolett.8b03559
Nano Lett. 2018, 18, 7794−7800

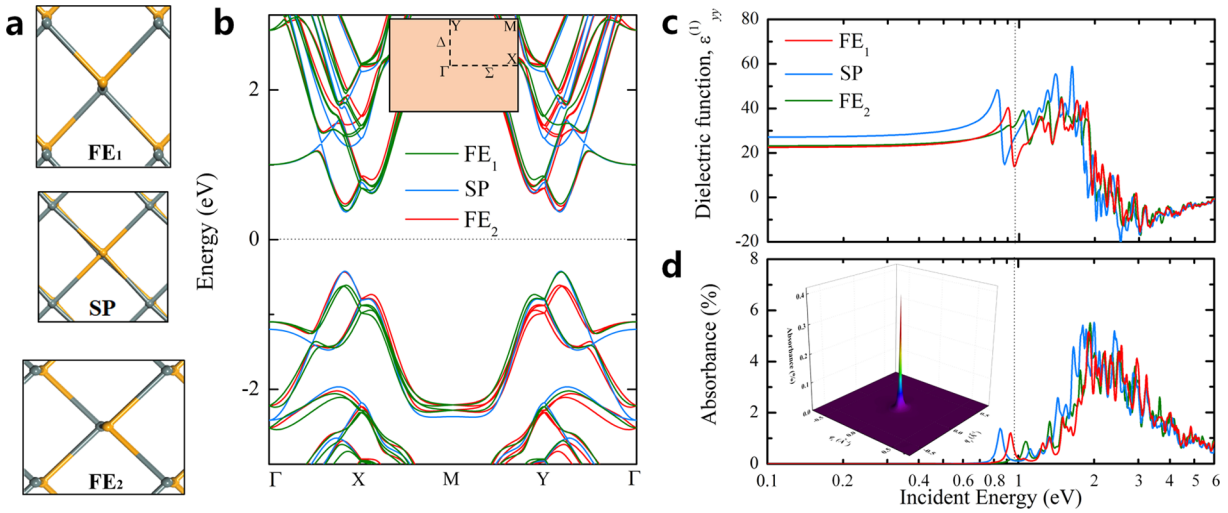

Figure 4. Optically driven phase transition of a SnSe monolayer. (a) The atomic structures of a SnSe monolayer in FE_1, FE_2, and SP states. (b) DFT-calculated band dispersions. Inset shows the first Brillouin zone of FE_1 orientation variant. (c) RPA calculated real part dielectric function $\varepsilon_{yy}^{(1)}$. (d) Optical absorbance spectra at the long wavelength limit ($q \rightarrow 0$). The vertical dashed line denotes an incident energy of 0.963 eV. Inset of (d) shows the absorbance of FE_1 in the whole k-space.

calculated long-wavelength dielectric function in the x-direction satisfies $\varepsilon_{FE_2}^{(1)}(\omega)|_{\omega<\omega_0} < \varepsilon_{SP}^{(1)}(\omega)|_{\omega<\omega_0} < \varepsilon_{FE_1}^{(1)}(\omega)|_{\omega<\omega_0}$, even below the indirect bandgap 2.92 eV. Therefore, one can also apply lower-frequency light to trigger phase transition while avoiding interband transitions.

For readout, one can use the transmission/reflection contrast for LPL. From Figure 2c we see that the biggest contrast occurs at $\hbar\omega_{readout}$ = 3.35 eV, for which there is a factor of 1.3 difference in reflectance between FE_1/FE_2, and optical absorption is marginal. At the GW-BSE level of theory, the readout energy can be selected as 4.46 eV with a factor of 2.2 change in reflectance. In addition, ferroelasticity can also be characterized by photothermal induced resonance technique, which has been applied to study anisotropic perovskites.[39]

SnO monolayers are centrosymmetric and have no polarization. In the following, we show that this scheme also works for a polarized 2D ferroelectric material. We consider a ferroelectric SnSe monolayer without centrosymmetry. It belongs to group-IV monochalcogenide family and has a simultaneous ferroelasticity and in-plane ferroelectricity.[40,41] Thus, SnSe monolayers have two equivalent orientation variants (Figure 4a), and each orientation variant has two internal polarizations. Previous work has found that tensile strain can switch between the two orientation variants of SnSe monolayers, and a static in-plane electric field can switch the polarization within one orientation variant.[20] Here we will show that a LPL pulse can transfer its orientation variant and consequently rotate its polarization $\mathbf{P}_0$ by 90°. In eq 1, the polarization $\mathbf{P}_0$ comes from noncentrosymmetric atomic structure. When the LPL frequency (on order of 10^2 THz) is much higher than phonon frequency (<6 THz, see Figure S1), the induced vibrational amplitude of ions excited at LPL frequency is small (Supporting Information). Therefore, the first term in eq 1 ($\mathbf{E}\cdot\mathbf{P}_0$) vanishes on time-averaging, even though $|\mathbf{P}_0|$ is finite.

We again focus on the electric field response of the electron subsystem. The pathway is from FE_1 to SP and then to FE_2, as shown in Figure 4a (and Figure S3 in Supporting Information). Our DFT calculations find that the lattice constant of FE_1 orientation variant is a = 4.275 Å, b = 4.401 Å, and for the SP $a = b$ = 4.312 Å, consistent with previous theoretical results.[20,40,41] The thickness of one SnSe monolayer is taken to be h = 5.895 Å. Hence, the 2D transformation strain tensors are $\eta_{FE_1} = \begin{pmatrix} -0.008 & 0 \\ 0 & 0.021 \end{pmatrix}$ and $\eta_{FE_2} = \begin{pmatrix} 0.021 & 0 \\ 0 & -0.008 \end{pmatrix}$. The SP state is energetically higher than the FE state by 1.76 meV/f.u. The DFT-calculated band dispersions are plotted in Figure 4b. We find that the FE structure ($pm2_1n$ layer group) is again a quasi-direct bandgap semiconductor. For the FE_1 orientation variant, the VBM is along the $\Gamma \rightarrow Y$ path (Δ = 0, 0.40 × $2\pi/b$, 0), and the CBM is along the $\Gamma \rightarrow X$ path (Σ = 0.42 × $2\pi/a$, 0, 0). The indirect bandgap is 0.82 eV. The direct bandgaps at the Δ and Σ points are 0.91 and 1.00 eV, respectively. At the many-body GW level of theory, these two direct bandgaps are 1.72 and 1.91 eV, respectively (Table S3). Group theory analysis reveals that the optical transition between the valence band and conduction band at the Δ point is allowed for y-polarized LPL and forbidden for x-polarized LPL (Table S2). These confirm that the electronic and optical transition properties of FE SnSe monolayer are anisotropic. The SP structure is a direct bandgap semiconductor (bandgap of 0.79 eV by DFT and 1.62 eV by GW), with degenerate extrema of the VBM and CBM at the Δ (0, 0.41 × $2\pi/b$, 0) and Σ (0.41 × $2\pi/a$, 0, 0) points, owing to its $cm2e$ layer group symmetry.

The RPA-calculated real part of dielectric functions in the y-direction of the three variants are shown in Figure 4c. At a selected incident energy, $\hbar\omega_0$ = 0.963 eV, the $\varepsilon_{yy}^{(1)}$ of FE_1, SP, and FE_2 are 14.14, 27.30, and 33.22, respectively. Therefore, according to our previous discussion, a LPL with electric field strength of E_0 = 0.29 V/nm is sufficient to demolish the energy barrier and switch the orientation variant athermally from FE_1 to FE_2 (Figure S3 in Supporting Information). The absorbance at this incident energy is very small (Figure 4d) with A = 0.5% in FE_1 and 0.1% in SP state, ensuring minimal parasitic absorption. We also calculate the dielectric function at the finite q (inset of Figure 4d). We find that the pronounced absorbance peak is at the Γ point, demonstrating that the indirect band transition is suppressed. The adiabatic energy

DOI: 10.1021/acs.nanolett.8b03559
Nano Lett. 2018, 18, 7794−7800

input limit is estimated to be 0.005 aJ/nm^3, smaller than that found above for a SnO monolayer. As with SnO, this OMT is a barrier-free, displacive transition, and its time scale is on the order of picoseconds. Due to the lack of elasticity constraints and tensile stresses (and associated damage), good reversibility can be expected. The optical response is also reproduced under GW-BSE calculation (Figure S4 in Supporting Information), where we observe higher contrast at an incident energy of $\hbar\omega_0$ = 1.51 eV. The calculated $\varepsilon_{yy}^{(1)}$ of FE_1, SP, and FE_2 are 3.85, 23.48, and 34.45, respectively. From these values we estimate a smaller laser power of $I_0 = 7.7 \times 10^9$ W/cm^2 and adiabatic energy input limit of 0.001 aJ/nm^3. From Figure 4c, one can use a readout energy $\hbar\omega_{readout}$ = 0.95 eV (or 1.58 eV according to GW-BSE level of theory) to yield a reflectance change of 1.5 (or 1.9 based on GW-BSE) between FE_1 and FE_2.

The laser driven SnSe monolayer orientation variant transition is interesting. As discussed previously, different orientation variants have distinct static polarizations. Hence we have shown that, using optical-frequency alternating electric field, one can modulate the electronic term (second order) to change the static polarization $\mathbf{P}_0$ in the first order term in Equation 1. That is, we can use oscillatory second-order term to tweeze ferroelectric domains.

Note that due to anisotropic feature of the FE 2D material, a LPL with its power lower than the critical power could also lift the FE_1 and FE_2 degeneracy and induce a phase transition with a reduced energy barrier. In Figure 5 we plot the variation of (a) energy difference between two FE states and (b) transition barrier with respect to electric field intensity of incident LPL. The energy barrier per area is evaluated by $E_b'/S = E_b/S - \frac{1}{2}(\varepsilon_{SP}^{(1)} - \varepsilon_{FE}^{(1)})h\varepsilon_0 E_0^2$. As the laser intensity increases, the FE_1 and FE_2 potential energy difference (transition energy barrier) increases (decreases) quadratically. These indicate that the phase transition could occur under moderate LPL exposure, even before the critical laser power proposed previously.

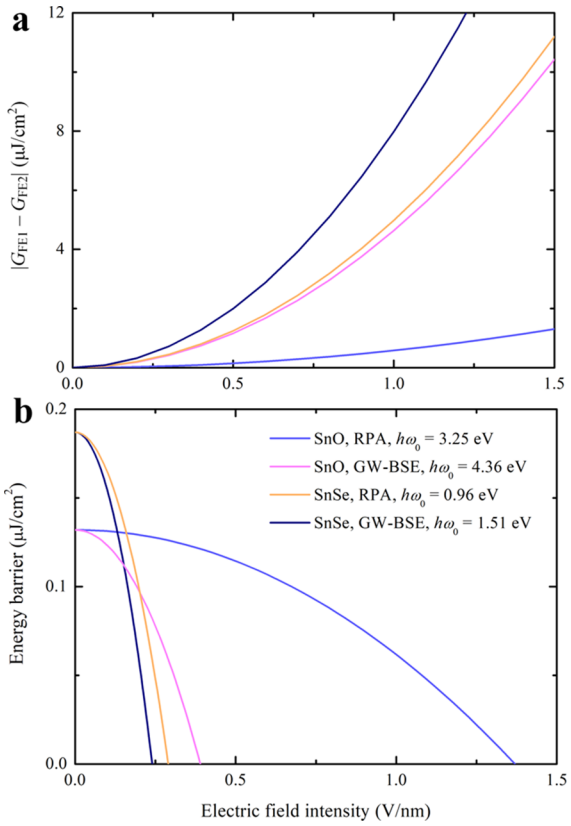

Figure 5. Variation of (a) FE_1/FE_2 grand potential difference and (b) transition energy barrier during phase transition as a function of incident LPL electric field intensity E_0.

One may wonder if such strategy can be applied to group-V monolayers, such as black phosphorus (α-P). Our calculations reveal that the energy barrier separating the two orientation variants of α-P monolayer is 238 meV/atom. This value is much larger than that in SnO and SnSe monolayer. Considering this, this opto-mechanical strategy is not suitable for α-P monolayer to switch between its ferroelastic variants.

In conclusion, we show that linearly polarized light provides a method to "tweeze" domain variant transitions in anisotropic 2D materials, akin to optical tweezers. These crystal structural transitions may occur within 1 ps throughout a macroscopic sample. Owing to this extraordinary speed, which approaches the upper limit of all possible atomic structural changes (e.g., one Debye oscillation period), the energy required for writing can be very small. Compared to orientation variant switching using static strain or static electric field, a laser-based scheme does not require mechanical, electrical, or electrochemical contact patterning, and could be preferable from cost considerations, especially for 2D materials which are highly optically addressable as they are "all surface". Opto-mechanical martensitic transitions (OMT) in 2D material do not suffer from the same elasticity constraint of martensitic transitions in 3D, because a freely suspended 2D membrane has no constraint in z. A small, −5% biaxial prebuckling (like a hammock) in x and y would ensure that subsequently no tensile stress will be generated during the OMT. Thereby, tensile stress-induced damage and long-term fatigue can be avoided: the OMT is expected to be highly reversible. All of our computed optical properties are consistent with more accurate many-body GW calculations, including exciton binding energy correction. Unlike the currently used chalcogenide Ge−Sb−Te alloys, the predicted structural transition is microscopically barrier-free and diffusionless, and thus exceptionally fast.

THEORETICAL METHODS

Density Functional Theory. Our first-principles calculations are based on density functional theory (DFT)[24,25] as implemented in the Vienna *ab initio* simulation package (VASP),[42,43] where the electron exchange-correlation interactions is treated by the generalized gradient approximation (GGA) functional in the Perdew−Burke−Ernzerhof (PBE) form.[44] The core and valence electrons are treated by projector augmented wave (PAW) method[45] and a planewave basis set, respectively. The kinetic cutoff energy for SnO and SnSe monolayers are set to be 520 and 350 eV, respectively. The in-plane lattice constants and atomic coordinates are fully relaxed using the conjugated gradient algorithm without applying any symmetry constraints. The convergence criteria for electronic and atomic relaxations are set to be 1×10^{-7} eV and 1×10^{-3} eV/Å, respectively. Each simulation supercell contains two chemical formula units (f.u.). The first Brillouin zone are sampled by a 15 × 15 × 1 Monkhorst−Pack **k**-point mesh,[46] whose convergence has been tested in a 19 × 19 × 1 mesh. We include self-consistent spin−orbit coupling effect in all calculations, which shows significant effects on the band

DOI: 10.1021/acs.nanolett.8b03559
Nano Lett. 2018, 18, 7794−7800

dispersion (Figure S5). The geometric structure, energy profile, and band dispersion agree well with previous calculations,[19,20,40,41] ensuring the accuracy of our simulation procedure. In order to analyze optical responses, we calculate the ion-clamped dielectric function according to random-phase approximation (RPA). More accurate quasi-particle GW calculations[30,31] with exciton binding correction (Bethe-Salpeter equation, BSE)[32,33] are also performed (Figure S6), giving qualitatively similar results compared with the RPA approach. Convergence tests of many-body calculations can be found in Table S4 and Table S5.

■ ASSOCIATED CONTENT

Supporting Information

The Supporting Information is available free of charge on the ACS Publications website at DOI: 10.1021/acs.nanolett.8b03559.

Coupling between linearly polarized light (LPL) and the ion sub-system; Energy analysis of barrier-free phase transition under LPL (PDF)

■ AUTHOR INFORMATION

Corresponding Author

*E-mail: liju@mit.edu.

ORCID

Jian Zhou: 0000-0002-2606-4833

Ju Li: 0000-0002-7841-8058

Notes

The authors declare no competing financial interest.

■ ACKNOWLEDGMENTS

This work was supported by an Office of Naval Research MURI through grant #N00014-17-1-2661. J. Z. thanks Dr. Ruixiang Fei for valuable simulation discussions.

■ REFERENCES

(1) Wuttig, M.; Yamada, N. *Nat. Mater.* **2007**, *6*, 824−832.
(2) Novoselov, K. S.; Geim, A. K.; Morozov, S. V.; Jiang, D.; Zhang, Y.; Dubonos, S. V.; Grigorieva, I. V.; Firsov, A. A. *Science* **2004**, *306*, 666−669.
(3) Novoselov, K. S.; Jiang, D.; Schedin, F.; Booth, T. J.; Khotkevich, V. V.; Morozov, S. V.; Geim, A. K. *Proc. Natl. Acad. Sci. U. S. A.* **2005**, *102*, 10451−10453.
(4) Wang, Q. H.; Kalantar-Zadeh, K.; Kis, A.; Coleman, J. N.; Strano, M. S. *Nat. Nanotechnol.* **2012**, *7*, 699−712.
(5) Li, L.; Yu, Y.; Ye, G. J.; Ge, Q.; Ou, X.; Wu, H.; Zhang, Y. *Nat. Nanotechnol.* **2014**, *9*, 372−377.
(6) Castro Neto, A. H.; Guinea, F.; Peres, N. M. R.; Novoselov, K. S.; Geim, A. K. *Rev. Mod. Phys.* **2009**, *81*, 109−162.
(7) Xu, X.; Yao, W.; Xiao, D.; Heinz, T. F. *Nat. Phys.* **2014**, *10*, 343−350.
(8) Mak, K. F.; He, K.; Shan, J.; Heinz, T. F. *Nat. Nanotechnol.* **2012**, *7*, 494−498.
(9) Xia, F.; Wang, H.; Jia, Y. *Nat. Commun.* **2014**, *5*, 4458.
(10) Fiori, G.; Bonaccorso, F.; Iannaccone, G.; Palacios, T.; Neumaier, D.; Seabaugh, A.; Banerjee, S. K.; Colombo, L. *Nat. Nanotechnol.* **2014**, *9*, 768−779.
(11) Qian, X.-F.; Liu, J.-W.; Fu, L.; Li, J. *Science* **2014**, *346*, 1344−1347.
(12) Feng, J.; Qian, X. F.; Huang, C. W.; Li, J. *Nat. Photonics* **2012**, *6*, 866−872.
(13) Li, Y.; Duerloo, K.-A. N.; Wauson, K.; Reed, E. J. *Nat. Commun.* **2016**, *7*, 10671.
(14) Kan, M.; Wang, J. Y.; Li, X. W.; Zhang, S. H.; Li, Y. W.; Kawazoe, Y.; Sun, Q.; Jena, P. *J. Phys. Chem. C* **2014**, *118*, 1515−1522.
(15) Li, W.; Li, J. *Nat. Commun.* **2016**, *7*, 10843.
(16) Wang, Y.; Xiao, J.; Zhu, H.; Li, Y.; Alsaid, Y.; Fong, K. Y.; Zhou, Y.; Wang, S.; Shi, W.; Wang, Y.; Zettl, A.; Reed, E. J.; Zhang, X. *Nature* **2017**, *550*, 487−491.
(17) Rehn, D. A.; Li, Y.; Pop, E.; Reed, E. J. *npj Comput. Mater.* **2018**, *4*, 2.
(18) Kundys, B.; Viret, M.; Colson, D.; Kundys, D. O. *Nat. Mater.* **2010**, *9*, 803−805.
(19) Seixas, L.; Rodin, A. S.; Carvalho, A.; Castro Neto, A. H. *Phys. Rev. Lett.* **2016**, *116*, 206803.
(20) Wu, M.; Zeng, X. C. *Nano Lett.* **2016**, *16*, 3236−3241.
(21) Li, L.; Chen, Z.; Hu, Y.; Wang, X.; Zhang, T.; Chen, W.; Wang, Q. *J. Am. Chem. Soc.* **2013**, *135*, 1213−1216.
(22) Daeneke, T.; Atkin, P.; Orrell-Trigg, R.; Zavabeti, A.; Ahmed, T.; Walia, S.; Liu, M.; Tachibana, Y.; Javaid, M.; Greentree, A. D.; Russo, S. P.; Kaner, R. B.; Kalantar-Zadeh, K. *ACS Nano* **2017**, *11*, 10974−10983.
(23) Ishii, A.; Li, J.; Ogata, S. *Int. J. Plast.* **2016**, *82*, 32−43.
(24) Hohenberg, P.; Kohn, W. *Phys. Rev.* **1964**, *136*, B864−B871.
(25) Kohn, W.; Sham, L. J. *Phys. Rev.* **1965**, *140*, A1133−A1138.
(26) Gajdoš, M.; Hummer, K.; Kresse, G.; Furthmüller, J.; Bechstedt, F. *Phys. Rev. B: Condens. Matter Mater. Phys.* **2006**, *73*, 045112.
(27) Ismail-Beigi, S. *Phys. Rev. B: Condens. Matter Mater. Phys.* **2006**, *73*, 233103.
(28) Qiu, D. Y.; da Jornada, F. H.; Louie, S. G. *Phys. Rev. B: Condens. Matter Mater. Phys.* **2016**, *93*, 235435.
(29) Laturia, A.; Van de Put, M. L.; Vandenberghe, W. G. *npj 2D Mater. Appl.* **2018**, *2*, 6.
(30) Hedin, L. *Phys. Rev.* **1965**, *139*, A796−A823.
(31) Hybertsen, M. S.; Louie, S. G. *Phys. Rev. Lett.* **1985**, *55*, 1418−1421.
(32) Salpeter, E. E.; Bethe, H. A. *Phys. Rev.* **1951**, *84*, 1232−1242.
(33) Onida, G.; Reining, L.; Rubio, A. *Rev. Mod. Phys.* **2002**, *74*, 601−659.
(34) Zhong, H.-X.; Gao, S.; Shi, J.-J.; Yang, L. *Phys. Rev. B: Condens. Matter Mater. Phys.* **2015**, *92*, 115438.
(35) Millar, R. W. *J. Am. Chem. Soc.* **1929**, *51*, 207−214.
(36) Marzari, N.; Mostofi, A. A.; Yates, J. R.; Souza, I.; Vanderbilt, D. *Rev. Mod. Phys.* **2012**, *84*, 1419.
(37) Mostofi, A. A.; Yates, J. R.; Lee, Y.-S.; Souza, I.; Vanderbilt, D.; Marzari, N. *Comput. Phys. Commun.* **2008**, *178*, 685−699.
(38) Shung, K. W.-K. *Phys. Rev. B: Condens. Matter Mater. Phys.* **1986**, *34*, 979.
(39) Strelcov, E.; Dong, Q.; Li, T.; Chae, J.; Shao, Y.; Deng, Y.; Gruverman, A.; Huang, J.; Centrone, A. *Sci. Adv.* **2017**, *3*, No. e1602165.
(40) Fei, R.; Kang, W.; Yang, L. *Phys. Rev. Lett.* **2016**, *117*, 097601.
(41) Shi, G.; Kioupakis, E. *Nano Lett.* **2015**, *15*, 6926−6931.
(42) Kresse, G.; Furthmüller, J. *Comput. Mater. Sci.* **1996**, *6*, 15−50.
(43) Kresse, G.; Furthmüller, J. *Phys. Rev. B: Condens. Matter Mater. Phys.* **1996**, *54*, 11169−11186.
(44) Perdew, J. P.; Burke, K.; Ernzerhof, M. *Phys. Rev. Lett.* **1996**, *77*, 3865−3868.
(45) Blöchl, P. E. *Phys. Rev. B: Condens. Matter Mater. Phys.* **1994**, *50*, 17953−17979.
(46) Monkhorst, H. J.; Pack, J. D. *Phys. Rev. B* **1976**, *13*, 5188−5192.

DOI: 10.1021/acs.nanolett.8b03559
Nano Lett. 2018, 18, 7794−7800

Supporting Information

Opto-mechanics driven fast martensitic transition in two-dimensional materials

Jian Zhou[1,2], Haowei Xu[1], Yifei Li[3], R. Jaramillo[3], Ju Li[1,3,*]

[1] Department of Nuclear Science and Engineering, Massachusetts Institute of Technology, Cambridge, MA 02139, USA

[2] Center for Advancing Materials Performance from the Nanoscale, State Key Laboratory for Mechanical Behavior of Materials, Xi'an Jiaotong University, Xi'an 710049, China

[3] Department of Materials Science and Engineering, Massachusetts Institute of Technology, Cambridge, MA 02139, USA

* E-mail address: liju@mit.edu

Coupling between linearly polarized light (LPL) and the ion sub-system.

We use photon-phonon interaction theory to evaluate the coupling between the laser and ionic sub-system. We note that the laser frequency (ω_0) proposed in the main text is on the order of 10^2 THz (for SnO ω_0 = 786 THz in RPA and 1028 THz in GW-BSE, and for SnSe ω_0 = 216 THz in RPA and 345 THz in GW-BSE), while the optical branch of phonon frequency ($\omega_{\mathbf{q}}$) is much lower (see Supplementary Figure S1, for SnO $\omega_{\mathbf{q}} < 16$ THz and for SnSe $\omega_{\mathbf{q}} < 6$ THz). In this way, conversation laws in inelastic photon-phonon scattering process yield $\omega = \omega_0 \pm \omega_{\mathbf{q}}$, and $\mathbf{K} = \mathbf{K}_0 \pm \mathbf{q}$. Here ω and $\mathbf{K}$ are frequency and wave vector of scattered light, respectively. Since $\omega_0 \gg \omega_{\mathbf{q}}$, and $K_0 = n \times \omega_0/c$ is very small (n is refraction index), then $K \approx K_0$ so that $q \approx 2 \times |\mathbf{K}_0| \times \sin(\theta/2)$. Then $q_{\max} = 2|\mathbf{K}_0| = 2 \times \sqrt{\varepsilon(\omega_0)} \times \omega_0/c$, which is on the order of 10^{-3} Å^{-1} (near the Γ point). Note that during the photon-phonon interaction, most of incident photons experience Rayleigh scattering, and only $\sim 10^{-7}$ of the intensity of the incident light are scattered inelastically (Brillouin scattering or Raman scattering). If one sheds laser for 10 ps on the sample, a few hundred

of photons hit each supercell (Supplementary Table S2). Hence, only < 10^{-4} photons experience inelastic scattering. This corresponds < 10^{-2} meV, which can be omitted in the analysis.

One can also apply classical driven oscillator model to estimate the ion response of laser. The equation of motion is

$$\frac{d^2\langle x\rangle}{dt^2}+2\zeta\omega_{ph}\frac{d\langle x\rangle}{dt}+\omega_{ph}^2\langle x\rangle=\frac{1}{\langle m\rangle}E_0\langle Q\rangle\sin\omega_0 t\ .$$

Here $\langle x\rangle$, $\langle m\rangle$, and $\langle Q\rangle$ are average values of displacement, mass, and charge of ion sub-system, respectively. In the steady state solution, the displacement amplitude is

$$\langle x\rangle_{\max}=\frac{\langle Q\rangle E_0}{\langle m\rangle\omega_0\sqrt{\left(2\omega_{ph}\zeta\right)^2+\left(\frac{\omega_{ph}^2-\omega_0^2}{\omega_0}\right)^2}}\ .$$

When $\omega_0 \gg \omega_{\mathrm{ph}}$, this gives $\langle x\rangle_{max}=\langle Q\rangle E_0/\langle m\rangle\omega_0^2$. We use Born effective charge Z^* to represent the $\langle Q\rangle$, then the amplitude is on the order of 10^{-6} Å for both SnO and SnSe monolayers. This also demonstrates that the coupling between laser and ionic sub-system can be omitted, and the ion contributed dielectric function within our concerned energy region is marginal. Hence, we only calculate the ion-clamped dielectric function in the main text.

Energy analysis of barrier-free phase transition under LPL.

Here we assume that the energy satisfies $U_{\mathrm{FE1}} = U_{\mathrm{FE2}} = U_{\mathrm{SP}}+E_{\mathrm{b}}$, where U is total energy per simulating supercell and E_{b} is positive, which serves as energy barrier separating two FE orientation variants. Under a LPL with electric field intensity E (e.g. along x-direction), barrier-free phase transition from $\mathrm{FE_1}$ to $\mathrm{FE_2}$ could occur under the following requirement:

$$-\frac{1}{2}\varepsilon_0\varepsilon^{(1)}_{\mathrm{FE}_2,xx}E^2Sh\le-\frac{1}{2}\varepsilon_0\varepsilon^{(1)}_{\mathrm{SP},xx}E^2Sh+E_b\le-\frac{1}{2}\varepsilon_0\varepsilon^{(1)}_{\mathrm{FE}_1,xx}E^2Sh\ ,$$

If $\varepsilon_{\mathrm{FE}_2}^{(1)} > \varepsilon_{\mathrm{SP}}^{(1)}$, the first inequality requires that $E^2 \geq \dfrac{2E_b}{\varepsilon_0 Sh\left(\varepsilon_{\mathrm{SP}}^{(1)} - \varepsilon_{\mathrm{FE}_2}^{(1)}\right)}$, which always holds;

If $\varepsilon_{\mathrm{FE}_2}^{(1)} < \varepsilon_{\mathrm{SP}}^{(1)}$, the first inequality requires that the field intensity satisfies $E^2 \leq E_{c,\max}^2 = \dfrac{2E_b}{\varepsilon_0 Sh\left(\varepsilon_{\mathrm{SP}}^{(1)} - \varepsilon_{\mathrm{FE}_2}^{(1)}\right)}$. $E_{c,\max}$ is maximum bound of electric field intensity, above which the SP structure has the lowest energy than those of FE_1 and FE_2 states (this is a volatile phase transition).

If $\varepsilon_{\mathrm{FE}_1}^{(1)} < \varepsilon_{\mathrm{SP}}^{(1)}$, then the second inequality takes the form of $E^2 \geq E_{c,\min}^2 = \dfrac{2E_b}{\varepsilon_0 Sh\left(\varepsilon_{\mathrm{SP}}^{(1)} - \varepsilon_{\mathrm{FE}_1}^{(1)}\right)}$, where $E_{c,\min}$ is the minimum bound of electric field intensity to obtain barrier-free phase transition.

If $\varepsilon_{\mathrm{FE}_1}^{(1)} > \varepsilon_{\mathrm{SP}}^{(1)}$, there is no solution.

To summarize, we can expect two cases to induce *barrier-free* phase transition from FE_1 to FE_2:

(i) $\varepsilon_{\mathrm{FE}_1}^{(1)} < \varepsilon_{\mathrm{FE}_2}^{(1)} < \varepsilon_{\mathrm{SP}}^{(1)}$, $E_{c,\min}^2 = \dfrac{2E_b}{\varepsilon_0 Sh\left(\varepsilon_{\mathrm{SP}}^{(1)} - \varepsilon_{\mathrm{FE}_1}^{(1)}\right)}$ and $E_{c,\max}^2 = \dfrac{2E_b}{\varepsilon_0 Sh\left(\varepsilon_{\mathrm{SP}}^{(1)} - \varepsilon_{\mathrm{FE}_2}^{(1)}\right)}$;

(ii) $\varepsilon_{\mathrm{FE}_1}^{(1)} < \varepsilon_{\mathrm{SP}}^{(1)} < \varepsilon_{\mathrm{FE}_2}^{(1)}$, $E_{c,\min}^2 = \dfrac{2E_b}{\varepsilon_0 Sh\left(\varepsilon_{\mathrm{SP}}^{(1)} - \varepsilon_{\mathrm{FE}_1}^{(2)}\right)}$ and there is no maximum bound of electric field intensity.

One should note that due to symmetry of two ferroelastic orientation variants, any finite electric field (even below critical intensity) could induce a phase transition from FE_1 to FE_2 with an energy barrier smaller than E_b.

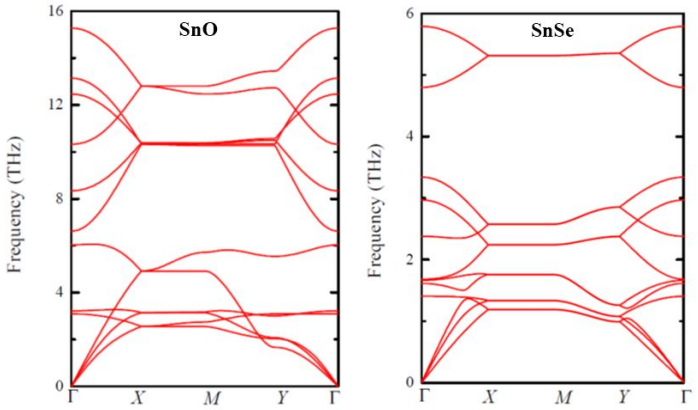

Figure S1. Phonon spectra of SnO (left panel) and SnSe (right panel) monolayers.

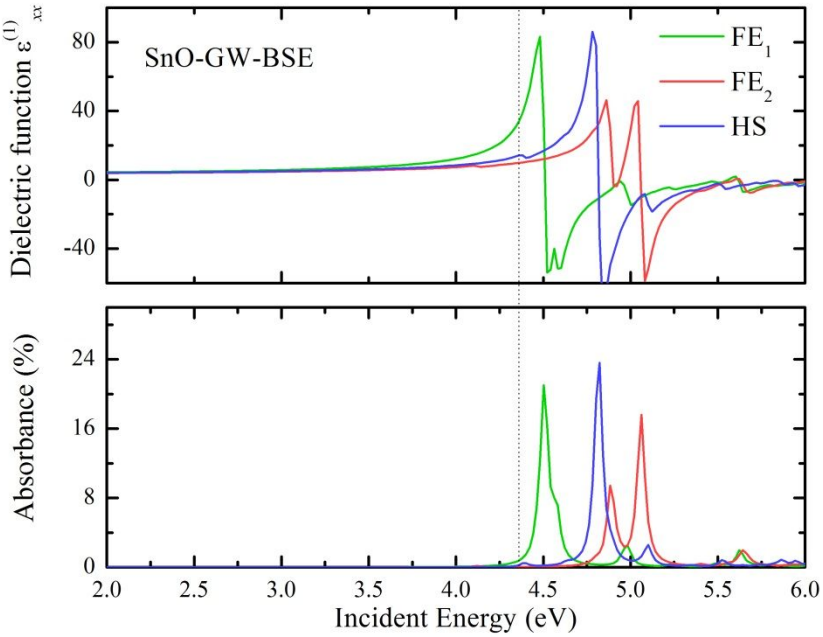

Figure S2. Real part of dielectric function and absorbance of SnO monolayer calculated by GW-BSE.

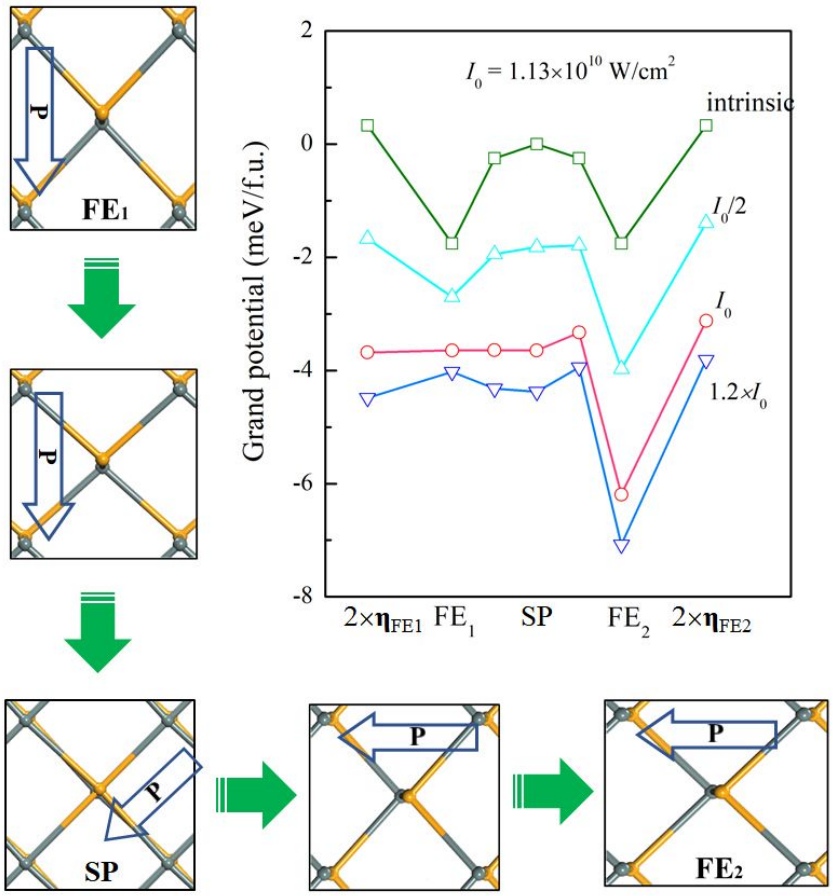

Figure S3. DFT calculated grand potential profile of SnSe monolayer per formula unit under different laser power. Polarization of each structure is also indicated.

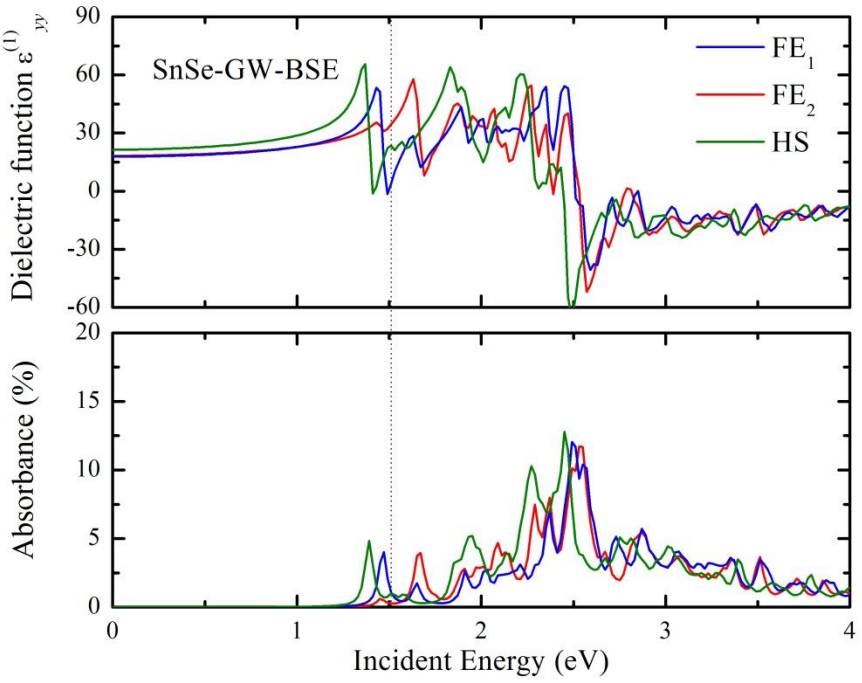

Figure S4. Real part of dielectric function and absorbance of SnSe monolayer calculated by GW-BSE.

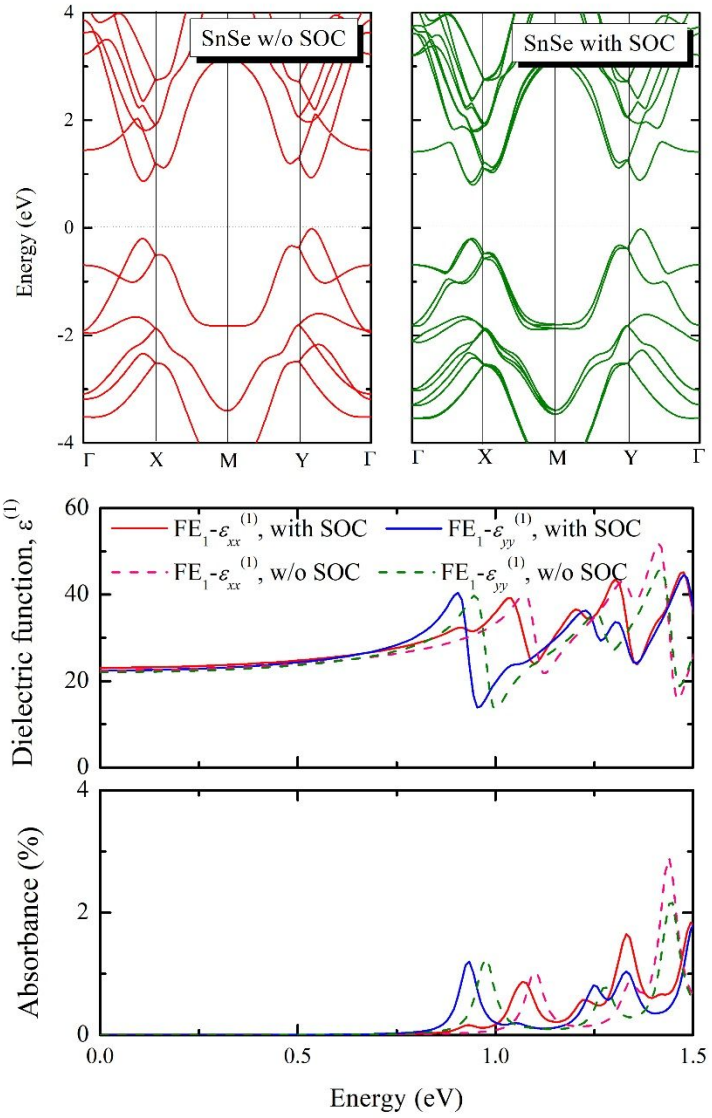

Figure S5. Band dispersion (upper panel) of a SnSe monolayer with and without including SOC effects. We can observe that SOC splits the doubly degenerated band, except along the Γ→Y path. This is due to mirror symmetry of M_x of the structure. At the X point, the valence band and conduction band exhibit 0.101 and 0.115 eV, respectively. DFT calculated dielectric function (middle panel) absorbance (lower panel) of a SnSe monolayer with and without SOC interactions.

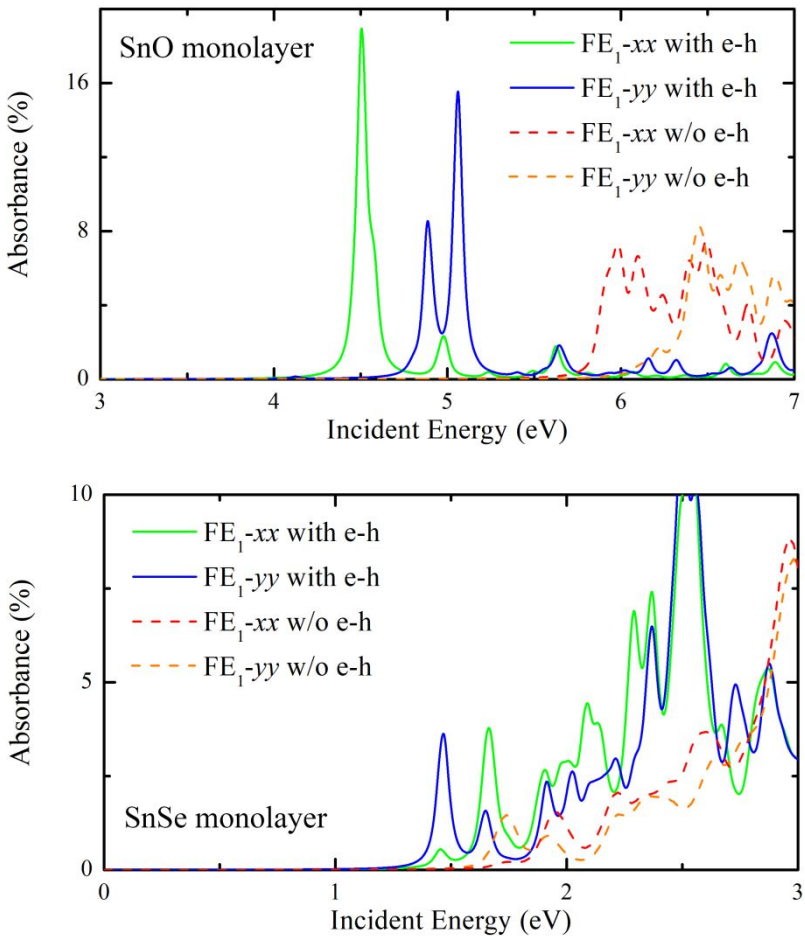

Figure S6. Absorbance of SnO and SnSe monolayers calculated under many-body GW calculations, with and without electron-hole pair interactions (BSE). The calculated exciton binding energies are listed in Table S3. The exciton binding energy of SnO monolayer is found to be anisotropic in the *xy* plane, while the SnSe monolayer shows isotropic exciton binding energy.

Table S1. Group representations of FE_1 SnO monolayer valence and conduction bands at high symmetric points Γ, X, M, and Y. The point group at these points are all C_{2v}. The calculations are under DFT level of theory. At the X, M, and Y points, the valence and conduction bands are both doubly degenerated. We also list the direct band gap and allowed linearly (*x* or *y*) optical transition at each point.

SnO (C_{2v})	Γ	X	M	Y
Direct band gap (eV)	3.11	3.45	3.57	3.99
valence band $\|u_{v,k}\rangle$	A_1	A_1, B_2	B_2, B_2	A_1, B_2
conduction band $\|u_{c,k}\rangle$	A_1	A_1, B_2	A_1, A_2	A_1, B_2
$\partial_{k_x}\|u_{v,k}\rangle$	B_2	B_2, A_1	A_2, A_1	B_2, A_2
$\partial_{k_y}\|u_{v,k}\rangle$	B_2	B_2, A_2	A_1, A_2	B_2, A_1
Allowed transition	none	*x*	*x*, *y*	*y*

Table S2. Group representations of FE_1 SnSe monolayer valence and conduction bands at points Σ (along Γ→X) and Δ (along Γ→Y) points. The point group at the Σ and Δ points are C_1 and C_s, respectively. The calculations are under DFT level of theory. The valence and conduction bands are both singly degenerated. We list the direct band gap and allowed linearly (*x* or *y*) optical transition at each point.

SnSe	Σ (C_1)	Δ (C_s)
Direct band gap (eV)	1.00	0.91
valence band $\|u_{v,k}\rangle$	A′	A′
conduction band $\|u_{c,k}\rangle$	A′	A′
$\partial_{k_x}\|u_{v,k}\rangle$	A′	A″
$\partial_{k_y}\|u_{v,k}\rangle$	A′	A′
Allowed transition	*x*, *y*	*y*

Table S3. Calculated parameters for SnO and SnSe phase transformation. Listed are DFT calculated lattice constants (a and b) in FE_1 orientation variant and SP state, energy barrier between FE_1 and FE_2 (E_b), direct band gap of FE_1 (E_g) in both DFT and GW calculations, Born effective charge along electric field direction (Z^*), exciton binding energy of FE_1 (E_{ex}) in GW with and without BSE, critical incident photon energy ($\hbar\omega_0$), electric field intensity (E_0), laser power (I_0) in both DFT and GW-BSE calculations, readout energy ($\hbar\omega_{readout}$), contrast in reflectance at readout energy (R_{FE1}/R_{FE2}), and adiabatic energy input limit (E_{input}).

	SnO monolayer	SnSe monolayer
a_{FE1} (Å)	3.656	4.275
b_{FE1} (Å)	4.028	4.401
$a_{SP} = b_{SP}$ (Å)	3.842	4.312
E_b (meV/f.u.)	0.61	1.76
E_g^{DFT} (eV)	3.11 (at Γ); 3.45 (at X) 3.57 (at M); 3.99 (at Y)	0.91 (at Δ); 1.00 (at Σ)
E_g^{GW} (eV)	6.20 (at Γ); 5.89 (at X) 6.31 (at M); 6.44 (at Y)	1.72 (at Δ); 1.91 (at Σ)
Z^* ($\|e\|$)	0.27 (Sn); –0.27 (O)	4.73 (Sn); –4.72 (Se)
E_{ex} (eV)	1.48 (along x); 1.56 (along y)	0.27 (along x); 0.27 (along y)
$\hbar\omega_0$ (eV)	3.25 (RPA); 4.36 (GW-BSE)	0.96 (RPA); 1.51 (GW-BSE)
E_0 (V/nm)	1.37 (RPA); 0.39 (GW-BSE)	0.29 (RPA); 0.24 (GW-BSE)
I_0 (W/cm^2)	2.53×10^{11} (RPA); 2.05×10^{10} (GW-BSE)	1.13×10^{10} (RPA); 7.7×10^{9} (GW-BSE)
$\hbar\omega_{readout}$ (eV)	3.35 (RPA); 4.46 (GW-BSE)	0.95 (RPA); 1.58 (GW-BSE)
R_{FE1}/R_{FE2}	1.3 (RPA); 2.2 (GW-BSE)	1.5 (RPA); 1.9 (GW-BSE)
E_{input} (aJ/nm^3)	0.07 (RPA); 0.006 (GW-BSE)	0.005 (RPA); 0.001 (GW-BSE)

Table S4. Convergence test of many-body calculation. We calculate the energy band gap and exciton binding energy with respect to *k*-mesh, number of bands, and cutoff energy. To obtain more accurate results, very dense *k*-mesh and cutoff energy are required. Here we show that our procedure converges values within 0.2 eV.

SnO monolayer	Band gap (eV)	Exciton B.E. (eV)
k-mesh (15×15×1); # of bands (64); energy cutoff (520 eV)	6.01	1.48
k-mesh (18×18×1); # of bands (64); energy cutoff (520 eV)	5.98	1.44
k-mesh (15×15×1); # of bands (128); energy cutoff (520 eV)	6.00	1.48
k-mesh (18×18×1); # of bands (96); energy cutoff (400 eV)	6.04	1.51

Table S5. Convergence test of many-body calculation for SnSe monolayer.

SnSe monolayer	Band gap at Γ (eV)	Exciton B.E. (eV)
k-mesh (15×15×1); # of bands (64); energy cutoff (350 eV)	1.75	0.27
k-mesh (12×12×1); # of bands (64); energy cutoff (350 eV)	1.77	0.31
k-mesh (18×18×1); # of bands (64); energy cutoff (350 eV)	1.73	0.25
k-mesh (15×15×1); # of bands (96); energy cutoff (350 eV)	1.75	0.27
k-mesh (18×18×1); # of bands (96); energy cutoff (320 eV)	1.74	0.28
k-mesh (18×18×1); # of bands (64); energy cutoff (400 eV)	1.71	0.23